Supercontinuum laser-based gonio-scatterometer for in and out-of-plane spectral BRDF measurements

François Margall, Gérald Lemineur, Romain Pacanowski, Sébastien Mavromatis, Eric Coiro, Alain Le Goff, Romain Ceolato

Research Article | Vol. 32, No. 15 / 15 Jul 2024 / Optics Express 25581
Optics EXPRESS

Supercontinuum laser-based gonio-scatterometer for in and out-of-plane spectral BRDF measurements

FRANÇOIS MARGALL,[1,2,3] GÉRALD LEMINEUR,[1] ROMAIN PACANOWSKI,[4] SÉBASTIEN MAVROMATIS,[3] ERIC COIRO,[2] ALAIN LE GOFF,[5] AND ROMAIN CEOLATO[1,*]

[1]ONERA, Université de Toulouse, Toulouse, France
[2]ONERA, Salon-de-Provence Air Base, France
[3]Aix-Marseille Univ, CNRS, LIS, Marseille, France
[4]INRIA, France
[5]DGA Information Superiority, Rennes, France
[*]romain.ceolato@onera.fr

Abstract: The hyperspectral component of bidirectional reflectance measurements, namely from several hundred wavelengths upwards, is attracting growing interest for numerous applications in both optics and computer graphics. In this paper, we present a motorized hyperspectral bidirectional reflectance measurement bench that performs in-plane and out-of-plane measurements for isotropic materials using a supercontinuum laser covering the visible and near infrared range, with a sub-nanometer spectral accuracy. We describe the complete data processing chain, including a method for assessing the alignment error of the measurement bench. From these measurements, we verify the principles of non-negativity, energy conservation and Helmholtz reciprocity. We introduce criteria also to evaluate the validity of the Lambertian hypothesis for the bidirectional reflectance and its deviation from reciprocity, obtained from the measurements directly. We show the need for spectral bidirectional reflectance measurements for certain materials, rejecting the separable function approximation.

1. Introduction

Hyperspectral imaging, enabled by the development of hyperspectral cameras [1], stands as a pivotal technology with diverse applications reaching beyond the traditional domain of computer graphics. The advances in research associated with this domain have also led to strong development in the field of hyperspectral rendering, that is used today to study aircraft signatures [2], perceptual research [3], target detection training [4], define instrument requirements [5] or as a tool for designers [6]. This variety in areas of use has been concurrent with the development of many different hyperspectral physically-based rendering engines [6–9], some of which can adapt to all types of scene, while others specialise in simulating target observation or predicting vehicle signatures [10–14], extending the spectral range beyond the visible by including part of the infrared spectrum. Taking the latter into account can also be used to study radiative transfer problems [15]. All these rendering engines, designed to produce physically realistic images, are dependent on the physical validity of the spectral bidirectional reflectances of the materials used [16]. As a consequence, it is necessary to be able to accurately measure the bidirectional reflectance of the materials involved in image rendering. However, while the literature is rich in measurement methods and databases of bidirectional reflectances measurements if one excludes taking wavelength into account [17], work on adding the spectral dimension, whether at the measurement or modelling level, is a more recent issue.

#520655 https://doi.org/10.1364/OE.520655
Journal © 2024 Received 6 Feb 2024; revised 3 Apr 2024; accepted 25 Apr 2024; published 2 Jul 2024

Optics EXPRESS

1.1. Context

Measuring the spectral bidirectional reflectance of materials can be done using several solution strategies such as image-based acquisition [18,19], allowing rapid acquisition time with high angular sampling, generally limited to a small number of wavelengths. The use of gonio-scatterometers, which greatly increase acquisition time but offer better angular accuracy, has also been developed in the literature [20,21]. This method, which can be used with a small number of wavelengths using different lasers [22], can also be coupled with the use of spectrometers and supercontinuum or uniform light sources [23–29], providing a much higher spectral definition than image-based acquisition systems. Other methods, such as Fourier optics instruments [6], allowing rapid measurement with high angular resolution but lower spectral definition, or using parabolic reflection [30] to enhance angular accuracy for curved surfaces measurements should also be noticed, among many others [31]. One solution developed by ONERA, MELOPEE [32], consisted of a bench for measuring in-plane hyperspectral bidirectional reflectances. Building upon these advancements, this study presents an innovative improvement to the existing setup ; This system, however, is subject to the same problems as the solutions already proposed in the literature. Three needs in particular have been identified and will be examined in this article:

I) a comprehensive methodology for ensuring the validity of measurements,

II) a generic method for studying and measuring the system alignment error,

III) a quantitative assessment criterion for the validity of a Lambertian model.

1.2. Objectives

The aim of developing a new hyperspectral bidirectional reflectance measurement bench is to be able to obtain output data whose physical validity is verified and whose measurement uncertainty is controlled. To achieve this, it is necessary to propose a robust processing chain that verifies and guarantees the physical properties of the measurements, such as non-negativity, conservation of energy and Helmholtz reciprocity principle. Since misalignment of the bench can cause systematic measurement bias, and the alignment of gonio-scatterometers after sample placement being an open problem in the literature, it is essential to provide a correction method for this problem. It would also be useful to be able to propose a criterion characterising the scattering behaviour of the sample that could be calculated from the measurement itself, in order to see whether the material behaves more specularly or diffusely as a function of wavelength. Such a criterion would also make it possible to check the validity of the separable function approximation.

1.3. Overview

The first part of this article, in Sec. 2.2, presents and details the design of our measurement bench and its functioning. We then, in Sec. 2.3.1, propose and describe a method for assessing the alignment error of the measurement bench in post-processing. Three Lambertian reference surfaces (LabSphere Spectralon) with reflectance values of 99%, 50% and 2% are studied, along with three vehicle paints. We then present the data processing chain applied to the measurements, proposing an ad hoc interpolation method that allows the calculation of specific quantities such as directional-hemispherical reflectance in Sec. 2.3.2. A description of the uncertainty in our results is given, both for direct measurements and for calculated quantities (Sec. 2.4). The results of the measurement bench are validated by verifying the non-negativity (Sec. 3.1), Helmholtz reciprocity principle (Sec. 3.2) and energy conservation (Sec. 3.3) of bidirectional reflectance for the samples measured, and by comparing the results with reference values. A new material characterisation criterion, the validity of the Lambertian hypothesis, is introduced (Sec. 3.4),

Optics EXPRESS

with the aim of proposing an efficient model for the bidirectional reflectance of measured samples in future work.

2. Method

2.1. Theoretical framework

Let $f(\omega_i, \omega_o, \lambda)$ be a function describing the spectral Bidirectional Reflectance Distribution Function (BRDF) of a material, where ω_i and ω_o are unit directions defined on the hemisphere Ω, such as $\omega_i := (\theta_i, \phi_i)$ and respectively $\omega_o := (\theta_o, \phi_o)$. As described by Nicodemus [33], the directions of incidence and observation can be reduced to three components such as $(\theta_i, \theta_o, \Delta\phi)$, where $\Delta\phi := \phi_o - \phi_i$ when considering an isotropic material, $\Delta\phi = 0$ corresponding to the incident plane in the specular direction. A spectral BRDF is said to be separable if it can verify the equality $f(\omega_i, \omega_o, \lambda) = f_\omega(\omega_i, \omega_o) f_\lambda(\lambda)$ for every configuration $(\omega_i, \omega_o, \lambda)$.

A physically plausible spectral BRDF must obey three properties: non-negativity (Eq. (1a)), energy conservation (Eq. (1b)) and Helmholtz reciprocity (Eq. (1c)).

$$\forall\ (\omega_i, \omega_o, \lambda), \qquad f(\omega_i, \omega_o, \lambda) \geqslant 0 \tag{1a}$$

$$\forall\ (\omega_i, \lambda), \qquad \int_\Omega f(\omega_i, \omega_o, \lambda)\ \cos\theta_o\, \mathrm{d}\omega_o \leqslant 1 \tag{1b}$$

$$\forall\ (\omega_i, \omega_o, \lambda), \qquad f(\omega_i, \omega_o, \lambda) = f(\omega_o, \omega_i, \lambda) \tag{1c}$$

Energy conservation can be verified by computing the Directional-Hemispherical Reflectance (DHR) of the spectral BRDF, denoted by ρ and explained in Eq. (2).

$$\forall\ (\theta_i, \lambda), \qquad \rho(\theta_i, \lambda) = \int_\Omega f(\omega_i, \omega_o, \lambda)\ \cos\theta_o\, \mathrm{d}\omega_o \tag{2}$$

For an isotropic material, Helmholtz reciprocity simplifies to $f(\theta_i, \theta_o, \Delta\phi, \lambda) = f(\theta_o, \theta_i, \Delta\phi, \lambda)$. However, in order to be able to study it statistically on our data sets, we introduce the reciprocity deviation criterion f_Δ, defined in Eq. (3), as the difference between the BRDF and its reciprocal value compared to their mean value. Perfect reciprocity results in $f_\Delta = 0$, while reciprocity for a case where one of the values is zero or tends towards infinity gives $f_\Delta = \pm 2$.

$$f_\Delta(\theta_i, \theta_o, \Delta\phi, \lambda) = 2\,\frac{f(\theta_i, \theta_o, \Delta\phi, \lambda) - f(\theta_o, \theta_i, \Delta\phi, \lambda)}{f(\theta_i, \theta_o, \Delta\phi, \lambda) + f(\theta_o, \theta_i, \Delta\phi, \lambda)} \quad | \quad f_\Delta \in [-2\,;2] \tag{3}$$

Independently of this criterion verifying the overall physical validity of the measurement, and in order to characterise the specular or diffuse property of the spectral BRDF, we propose a criterion that models the validity of the Lambertian hypothesis for the material, denoted Λ, given in Eq. (4). By definition, this criterion has a value between 0 and 1, 1 corresponding to a perfect Lambertian BRDF whereas 0 corresponds to a BRDF proportional to a Dirac distribution. The derivation of these values is shown in Supplemental Document 1.

$$\Lambda(\theta_i, \lambda) = 1 - \frac{\int_\Omega |f(\omega_i, \omega_o, \lambda) - \rho(\theta_i, \lambda)/\pi|\, \cos\theta_o\, \mathrm{d}\omega_o}{2\,\rho(\theta_i, \lambda)} \quad | \quad \Lambda \in [0\,;1] \tag{4}$$

It should be noted that while this criterion judges the effectiveness of a Lambertian model of the material as a function of incidence and wavelength, it is not directly appropriate for studying the specular part of the BRDF only. This point is investigated and discussed in more detail in Sec. 4.1.

Optics EXPRESS

2.2. Measurement bench

The spectral BRDF measurement bench MELOPEE NG (for Next Generation), developed at ONERA, consists of two motorized arms, one for a supercontinuum laser Leukos STM 250-VIS-IR and the other for a spectrometer Avantes AvaSpec HS-TEC with a spectral observation range of [450 nm, 1100 nm] with a resolution of less than a nanometer. A more complete description of the components used in the measurement bench is given in Fig. 1.

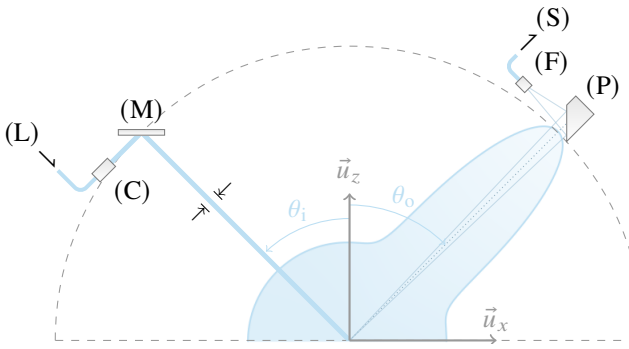

Fig. 1. Optical diagram of the measurement bench. The emitting arm consists of a Leukos STM 250-VIS-IR supercontinuum laser (L) transported in an optical fibre, collimated by a custom-made collimator from Leukos (C) and then redirected towards the sample by a mirror (M). Emissive beam has a diameter ϕ = 5.0 mm. The sensor arm consists of a Thorlabs MPD129-P01 off-axis parabolic mirror (P) that reflects the collected light back to an optical fibre (F), which is connected to an Avantes AvaSpec HS-TEC spectrometer (S).

As shown in the schematic diagram Fig. 2(a), the carrier arm of the supercontinuum laser has one degree of freedom, enabling it to move the light source in the plane by an angle θ_i ranging from $-90°$ to $90°$. As the incident beam has a diameter of ϕ = 5.0 mm, the theoretical maximum angle of incidence is 84.26° for a 5 cm square sample, and can reach 88.08° for a 15 cm square sample, the maximum size supported by the measurement bench. The spectrometer support arm has two degrees of freedom, θ_o ranging from 0° to 90° and $\Delta\phi$ from 0° to 360°. Two blind zones exist: the first in the backscatter area and the second one when $\{\theta_o \geqslant 25°, 205° \leqslant \Delta\phi \leqslant 290°\}$. Each arm is driven by a motor with an angular accuracy of 0.001°. The light reflected by the sample in the direction of observation is collected by an off-axis parabolic mirror with a cross-section radius of 1.01°, corresponding to a solid angle of 9.77×10^{-4} sr (giving a theoretical maximum observation zenith angle θ_o of almost 89°). This result is obtained by calculating the solid angle of the surface resulting from the intersection between the acceptance cone of the optical fibre, noted (F) in Fig. 1, and the surface of the off-axis mirror, noted (P). The calculation is explained in Supplemental Document 1. This value can be reduced if needed by adding a diaphragm.

The value of the measured spectral BRDF $f_m(\theta_i, \theta_o, \Delta\phi, \lambda)$ is calculated using Eq. (5), where $I_m(\theta_i, \theta_o, \Delta\phi, \lambda)$ corresponds to the raw measurement of the material, $I_{m,c}(\theta_o, \Delta\phi, \lambda)$ being the raw measurement of the calibration sample material (LabSphere SRS-99-010), and f_c its associated known spectral BRDF, in practice a function depending only on λ, the calibration sample being assumed to be Lambertian. The curve associated with the calibration function $f_c(\lambda)$ is shown in Supplement 1.

$$f_m(\theta_i, \theta_o, \Delta\phi, \lambda) = \frac{I_m(\theta_i, \theta_o, \Delta\phi, \lambda)}{I_{m,c}(\theta_o, \Delta\phi, \lambda)} f_c(\lambda) \tag{5}$$

The sampling step for the ω_o observation directions depends on the deviation from the specular direction $\omega_s := (\theta_i, 0)$, delimiting the observation space into three zones centred on ω_s. The

Optics EXPRESS

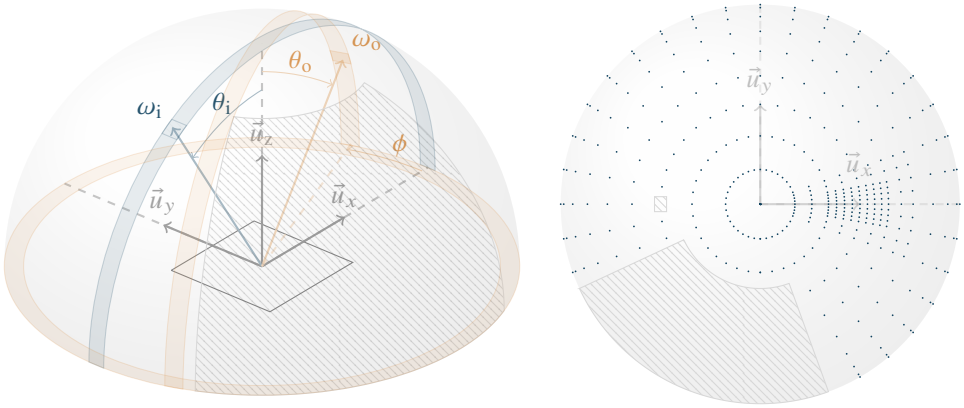

(a) (b)

Fig. 2. (a) Schematic diagram of the measurement bench. The blue band represents the degree of freedom of the supercontinuum laser, while the orange bands depict the two degrees of freedom of the sensor. The hatched areas represent blind zones unreachable for the latter. (b) Example of a sampling pattern of observation directions, here for an incident angle $\theta_i = 30°$.

limiting distance to ω_s separating these zones, defined as $d_\infty(\omega_s, \omega_o) = \max(|\theta_i - \theta_o|, |\Delta\phi|)$, generally called Chebyshev distance or L_∞-metric [34], and the sampling for each zone is up to the experimenter. An example of the sampling of observation directions on the hemisphere is shown in Fig. 2(b).

2.3. *Data processing*

The processing chain applied to the measurements is shown in Fig. 3. Non-negativity and reciprocity are systematically checked for each measurement, with the constraint of measuring the sample at a minimum of two incidences for the latter. These computations are carried out on the raw data without applying any modification. Before applying any changes to the data, an alignment study is carried out, since misalignment can introduce a systematic bias into our measurements. A method for determining the alignment error is proposed and detailed in Sec. 2.3.1.

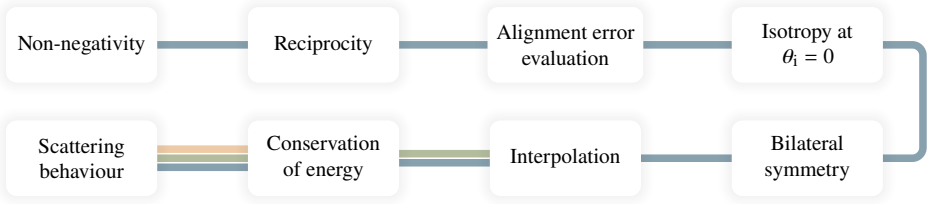

Fig. 3. Summary diagram of post-processing steps carried out on measurement bench output data. The input data required at each stage is represented by the pipelines: blue requires at least the raw dataset, green requires the complete dataset after interpolation, and orange represents the DHR as a prerequisite.

Although the measurement bench is not designed to study anisotropic materials, we still can check the BRDF slice for possible anisotropy at normal incidence. Bilateral symmetry (i.e. incident plane symmetry), as defined by Romeiro et al. [35], such as $\Delta\phi := |\phi_o - \phi_i|$, is

Optics EXPRESS

studied for compatible measurement zones. The missing measurements from the blind zone are reconstructed from the complementary measurements if the bilateral symmetry is verified. The data is then interpolated in the last missing zones, such as grazing angles or backscatter using the method described in Sec. 2.3.2, so that the DHR can then be calculated to verify energy conservation. Finally, the DHR is used to calculate the validity of the Lambertian hypothesis for the material under study.

2.3.1. Alignment error analysis

The alignment of gonio-scatterometers is an inherent difficulty in this type of optical setup, and although several methods exist [28,36], they are based on alignment before the measurement sample is placed. We propose here a method applied as a post-process for determining the alignment error.

We consider two errors inherent in our measurement after placing the sample on the setup: a vertical alignment error Δz, positioning the sample surface above or below the collimation point of the two arms, and an orientation error on the normal of the sample surface $\omega_\mathrm{n} := (\theta_\mathrm{n}, \phi_\mathrm{n})$. It is assumed that the maximum value of the BRDF is observed in the true specular direction: this assumption, which may be false at large angles of incidence, implies that we must limit ourselves to a study of the alignment error at low incidences.

Noting l_c the distance between the sensor and the theoretical collimation point, θ_i the theoretical angle of incidence and $(\theta_\mathrm{o}, \Delta\phi)$ the direction of observation of the assumed specular peak, the relationship between the quantities Δz and ω_n is given in Eq. (6), which is demonstrated in the Supplement 1, together with the derivation of the terms $\tau(\omega_\mathrm{n})$ (Eq. (7)) and $\omega_\mathrm{r} := 2\,(\omega_\mathrm{i} \cdot \omega_\mathrm{n})\,\omega_\mathrm{n} - \omega_\mathrm{i}$, which is defined as the specular reflection occurring on the actual macroscopic surface of the sample.

$$\Delta z(\omega_\mathrm{n}) = l_\mathrm{c} \left[\cos\theta_\mathrm{o} \frac{\omega_\mathrm{r}(\omega_\mathrm{n}) \cdot u_x}{\omega_\mathrm{r}(\omega_\mathrm{n}) \cdot u_z} - \sin\theta_\mathrm{o} \cos\Delta\phi \right] \frac{\omega_\mathrm{r}(\omega_\mathrm{n}) \cdot u_z \, \tau(\omega_\mathrm{n}) \cos\theta_\mathrm{i} \sin\theta_\mathrm{i}}{\omega_\mathrm{r}(\omega_\mathrm{n}) \cdot (u_x \sin\theta_\mathrm{i} + u_z \cos\theta_\mathrm{i})} \tag{6}$$

$$\tau(\omega_\mathrm{n}) = \frac{1}{\cos\theta_\mathrm{i} - \sin\theta_\mathrm{i} \tan\theta_\mathrm{n} \cos\phi_\mathrm{n}} \tag{7}$$

Since the value of ϕ_n can be obtained by observing the azimuthal position of the specular peak at normal incidence, Eq. (6) can be reduced to a simple $\Delta z(\theta_\mathrm{n})$ relationship. By plotting this relationship for each incidence, we obtain characteristic curves such as those shown in Fig. 4, generated from a simulated BRDF dataset with a chosen alignment error.

These curves intersect each other around a single point, allowing us to deduce a confidence interval for the values of Δz and θ_n. The mean and standard deviation of the abscissa and ordinate of the intersection points are calculated to obtain θ_n and Δz respectively, weighted using w_n and $w_{\Delta z}$ defined in Eqs. (8a) and (8b), with Δz_1 and Δz_2 being the intersecting curves and $\theta_{1,2}$ the abscissa of the point of intersection. This weighting allows the local tangent to be taken into account, with a horizontal tangent providing better accuracy for Δz, while a vertical tangent favours the determination of θ_n.

$$w_\mathrm{n} = \max\left\{ \frac{2}{\pi} \arctan\left[\frac{\partial \Delta z_1}{\partial \theta_\mathrm{n}}(\theta_{1,2}) \right], \frac{2}{\pi} \arctan\left[\frac{\partial \Delta z_2}{\partial \theta_\mathrm{n}}(\theta_{1,2}) \right] \right\} \tag{8a}$$

$$w_{\Delta z} = 1 - \min\left\{ \frac{2}{\pi} \arctan\left[\frac{\partial \Delta z_1}{\partial \theta_\mathrm{n}}(\theta_{1,2}) \right], \frac{2}{\pi} \arctan\left[\frac{\partial \Delta z_2}{\partial \theta_\mathrm{n}}(\theta_{1,2}) \right] \right\} \tag{8b}$$

Applying this method to the simulated data shown in Fig. 4, we derive the following alignment errors from datasets for four different incidences: $\theta_\mathrm{n} = (0.935 \pm 0.034)^\circ$, $\phi_\mathrm{n} = (4.0 \pm 0.1)^\circ$, $\Delta z = (2.67 \pm 2.60)$ mm.

Optics EXPRESS

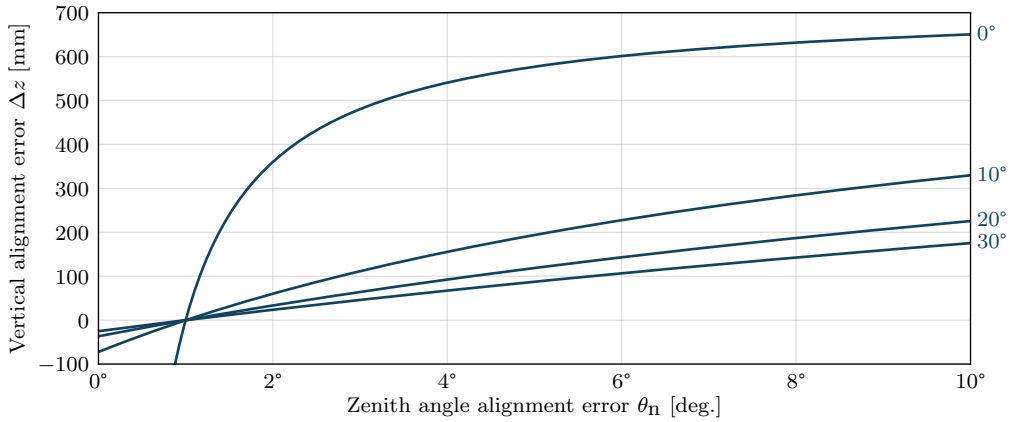

Fig. 4. Alignment curves obtained from BRDF data simulated using a Blinn-Phong model [37] with a uniform error of ± 4.3% and an alignment error of $\Delta z = +1.2$ mm, $\theta_n = 0.9°$, $\phi_n = 3.6°$, using four different θ_i incident angles. The slope of the curves at the intersection point, generally close to the horizontal, improves accuracy on θ_n but reduces it on Δz.

The results presented here are representative of the method. Because of the behaviour of the alignment curves $\Delta z(\theta_n)$ for low values of θ_n, which generally have a high slope, we systematically obtain low accuracy for the vertical alignment error Δz, coupled with good accuracy for the angular alignment error ω_n. Since the vertical alignment error can be estimated on the measurement bench (with an uncertainty of around ±2 mm), the method provides interest for the estimation of (θ_n, ϕ_n), for which we have no other estimation method.

2.3.2. BRDF interpolation

Various methods for interpolating BRDF measurements can be found in the literature [19,38,39], each responding to a particular problem. Our specific needs are for an interpolation method that can handle a non-regular data grid, retains the physical plausibility criteria of the BRDF, respects its topology and is computationally not too expensive, with no need to take anisotropy into account.

We therefore use an interpolation method based on radial basis functions (RBF) with a Gaussian kernel of the form $\exp\left(-\text{dist}\left(\omega_1, \omega_2\right) / \epsilon_d\right)^2$, dist being the metric associated to the topological space of the BRDF (as shown in Eq. (9), $\text{hav}\left(\theta\right) := \sin^2\left(\theta/2\right)$ representing the haversine function) and ϵ_d being the average distance between nodes. The choice of kernel is important, and using a Gaussian allows us to benefit from important properties: the assurance of non-negativity, the uniqueness of the interpolation, a smooth function by construction (i.e. of class C^∞), among others [40].

$$\text{dist}\left(\omega_1, \omega_2\right) := 2 \arcsin\left\{\left[\text{hav}\left(\theta_2 - \theta_1\right) + \sin\theta_1 \sin\theta_2 \text{hav}\left(\Delta\phi_2 - \Delta\phi_1\right)\right]^{1/2}\right\} \tag{9}$$

In order to avoid extrapolation problems at large observation angles, we will interpolate these zones before any other processing in the space of the $f\left(\omega_i, \omega_o\right)\cos\theta_o$, in order to know its limit value, by definition $\lim_{\theta_o \to \pi/2} f\left(\omega_i, \omega_o\right)\cos\theta_o = 0$. Bilateral symmetry, if verified in areas where it is measurable, can also be applied to reduce the areas to be interpolated.

2.4. Uncertainty analysis

In addition to the estimation of the angular error due to alignment bias presented in Sec. 2.3.1, the uncertainty in the BRDF measurement must be taken into account.

Optics EXPRESS

Assuming that each term is decorrelated from the others in the expression of the measured BRDF (Eq. (5)), we can define the general value of uncertainty by adding in quadrature first-order linear contributions of each variable [41], giving us the result shown in Eq. (10).

$$\begin{aligned}\Delta f_{\mathrm{m}} &= \left[\left(\frac{\partial f_{\mathrm{m}}}{\partial I_{\mathrm{m}}}\right)^2 \Delta I_{\mathrm{m}}^2 + \left(\frac{\partial f_{\mathrm{m}}}{\partial I_{\mathrm{m,c}}}\right)^2 \Delta I_{\mathrm{m,c}}^2 + \left(\frac{\partial f_{\mathrm{m}}}{\partial f_{\mathrm{c}}}\right)^2 \Delta f_{\mathrm{c}}^2\right]^{1/2} \\ &= f_{\mathrm{m}} \left(2\sigma_{\mathrm{m}}^2 + \sigma_{\mathrm{c}}^2\right)^{1/2}\end{aligned} \tag{10}$$

By calculating σ_{m} the raw measurement uncertainty such as $\sigma_{\mathrm{m}} = (\sigma_{\mathrm{l}}^2 + \sigma_{\mathrm{s}}^2)^{1/2}$ where σ_{l} and σ_{s} represent respectively the uncertainties of the light source power and the one of the sensor, and with σ_{c} the uncertainty of the reflectance calibration sample material, all of the given by the manufacturers, we can have access to the uncertainty of our measurement. The numerical results of the uncertainty calculations are shown in Table 1. These results are obtained without repeating the measurement, as the spectrometer's integration time adapts to the amount of flux received depending on the sample and the bidirection.

Table 1. List of uncertainties used to calculate the relative uncertainty of the BRDF.

	Absolute uncertainty		Relative uncertainty		Contribution to total	
Wavelength [nm]	450-600	601-1100	450-600	601-1100	450-600	601-1100
Spectralon DHR	0.0053	0.0049	± 0.50 %	± 0.54 %	9.2 %	9.8 %
Laser	—	—	± 3 %		13.0 %	12.9 %
Sensor	—	—	± 0.5 %		77.8 %	77.3 %
Total			± 4.3 %		100.0 %	100.0 %

2.4.1. Numerical integration uncertainty

In order to calculate both the DHR and the validity of the Lambertian hypothesis, it will be necessary to calculate the spectral BRDF integral numerically. Given the irregular nature of our angular sampling (as shown in Fig. 2(b)), we will use Simpson's composite method for irregular spaced data [42].

Although the inherent error is known for a number of Simpson's methods [43], to our knowledge the error associated with this one has never been derived in the literature. As derived in Supplement 1, it can be demonstrated that the inherent error associated with this method for a sub-interval h_n is as shown in Eq. (11), where the symbol $\Delta^k f_n$ represents the divided difference at k-th order of the n-th value from a data set f, h_n being the sub-interval between the coordinates associated to the points f_n and f_{n+1}.

$$E = -\frac{(h_n - h_{n-1})(h_n + h_{n-1})^3}{144}\left(\Delta^3 f_{n-1} + \Delta^3 f_{n-2}\right) \tag{11}$$

However, this inherent error remains small compared to the propagation of uncertainty through numerical integration. To look further at the calculation of this uncertainty, we invite the reader to turn again to Supplement 1 for a complete explanation and derivation of this error.

3. Results

Four samples with reference DHR are used in this article: three Labsphere Spectralon, references SRS-99-010, SRS-50-010 and SRS-02-010 (hereafter referred to as SRS99, SRS50 and SRS02 respectively) and a green paint for vehicles, reference 34X3. Photographs of the samples are shown in Table 2.

Optics EXPRESS

Table 2. Images of the four samples measured and studied. The length scale is in cm. Two additional vehicle paint samples are studied and shown in Supplement 1.

34X3	SRS99	SRS50	SRS02

Additional measurements, carried out on two vehicle paint samples from the manufacturer Stardust Colors, are presented in Supplement 1.

3.1. Spectral BRDF measurements

The processing chain produces a complete dataset after interpolation. In addition, once bilateral symmetry had been verified in the compatible measurement zones, the blind zones defined in Fig. 2 were reconstructed. An example of the data obtained, in this case for sample 34X3, is shown in Fig. 5. The data in Fig. 5(a) represent a measurement of BRDF after treatment at incidence and fixed wavelength as a function of $(\theta_o, \Delta\phi)$, while Fig. 5(b) shows the BRDF at fixed incidence and azimuth in the plane of incidence, as a function of (θ_o, λ). The corresponding graphs for the additional samples can be found in Supplemental Document 1. Graphs representing the same quantities were plotted for samples SRS99, SRS50 and SRS02, and are shown in Fig. 6. Additional graphs of BRDF measurements on these samples with a scale focused on each dataset are also presented in Supplement 1.

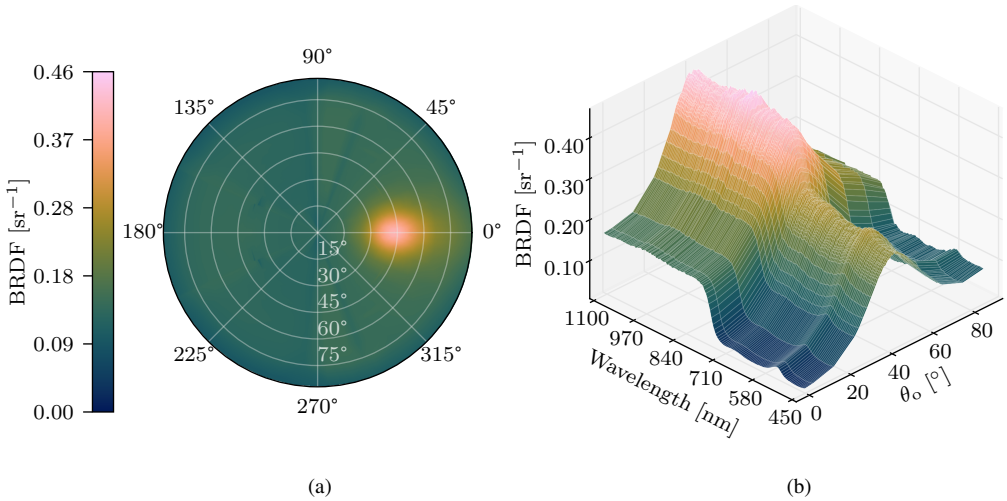

(a) (b)

Fig. 5. (a) In and out-of-plane BRDF measurements of sample 34X3 for $\theta_i = 40°$ and $\lambda = 780$ nm. (b) In-plane BRDF measurements of sample 34X3 for $\theta_i = 40°$ and various wavelengths. Figure (b) shows a variation in the shape of the BRDF lobe as a function of wavelength, rendering a separable function model $f(\omega_i, \omega_o, \lambda) = f_\omega(\omega_i, \omega_o) f_\lambda(\lambda)$ unsuitable.

The results of the spectral BRDF measurements shown here are presented without applying a correction linked to the estimation of the alignment error as shown in Sec. 2.3.1. For a

Optics EXPRESS

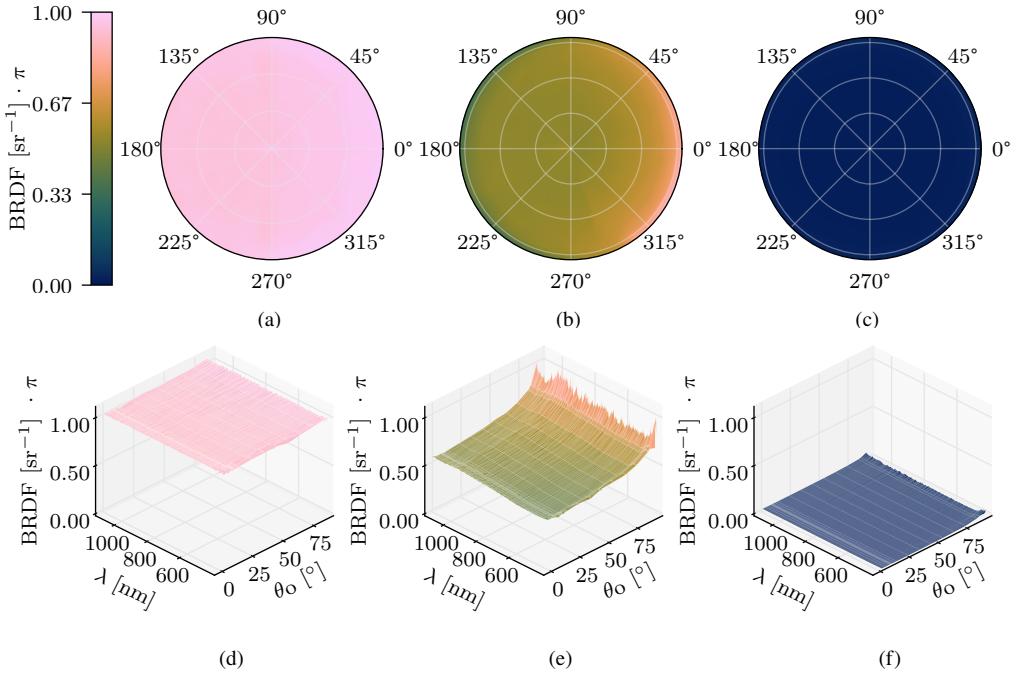

Fig. 6. BRDF measurements after treatment for samples SRS99 (a, d), SRS50 (b, d) and SRS02 (c, f). The BRDF scale is normalised by multiplying it by π. (First row) Out-of-plane measurements for a wavelength $\lambda = 780$ nm with an incident angle $\theta_i = 8°$. (Second row) In-plane measurements with an incident angle $\theta_i = 8°$. Additional figures at a scale specific to each sample are presented and discussed in the Supplement 1.

presentation of the results obtained using this method and a discussion of its use, we invite the reader to refer to Sec. 4.1.

3.2. *Helmholtz reciprocity*

The study of Helmholtz reciprocity is made for each sample for bidirections in and out of the plane of incidence, for zenith angles of up to $\theta_o = 60°$, and is presented in Figs. 7 and 8: Fig. 7 shows the relationship between the values measured in reciprocal BRDF bidirections as a function of wavelength, the deviation from reciprocity being defined according to Eq. (3). The distribution of reciprocity deviation values is also shown in the same figure on the right part. The latter presents the results obtained for sample 34X3 only: the reader can find the graphs corresponding to the other samples by referring to Supplement 1.

The left part on Fig. 7 shows all the reciprocal bidirections $(\theta_i, \theta_o, \Delta\phi, \lambda)$ and $(\theta_o, \theta_i, \Delta\phi, \lambda)$, the colour of each point representing the wavelength of observation λ, its coordinates being given by the measurements $f(\theta_i, \theta_o, \Delta\phi, \lambda)$ and $f(\theta_i, \theta_o, \Delta\phi, \lambda)$. Perfect reciprocity places the corresponding point on the central horizontal line.

For each material, the distributions of absolute values of deviation from reciprocity $|f_\Delta|$ are used to calculate their associated Cumulative Distribution Functions (CDFs) for each wavelength, as shown in Fig. 8(a). Integrating the Complementary Cumulative Distribution Function (CCDF, defined as one minus CDF) for each wavelength gives us an effective indicator of the variation in reciprocity as a function of wavelength (Fig. 8(b)).

Optics EXPRESS

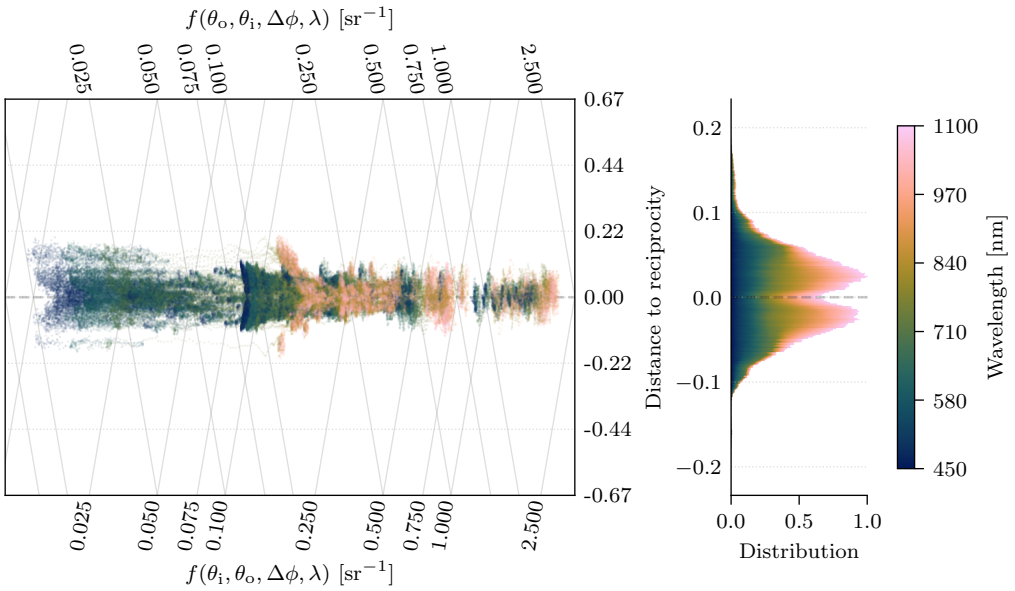

Fig. 7. Helmholtz reciprocity studied for sample 34X3. Deviation from reciprocity is calculated according to the metric noted in Eq. (3). The deviation from reciprocity is low, with an increase for low BRDF values, which can be explained by greater measurement noise. The distribution is not centered, revealing a measurement bias due to alignment error, calculated in Sec. 4.1 using the method presented in Sec. 2.3.1. Equivalent figures for Spectralons are presented and discussed in Supplement 1.

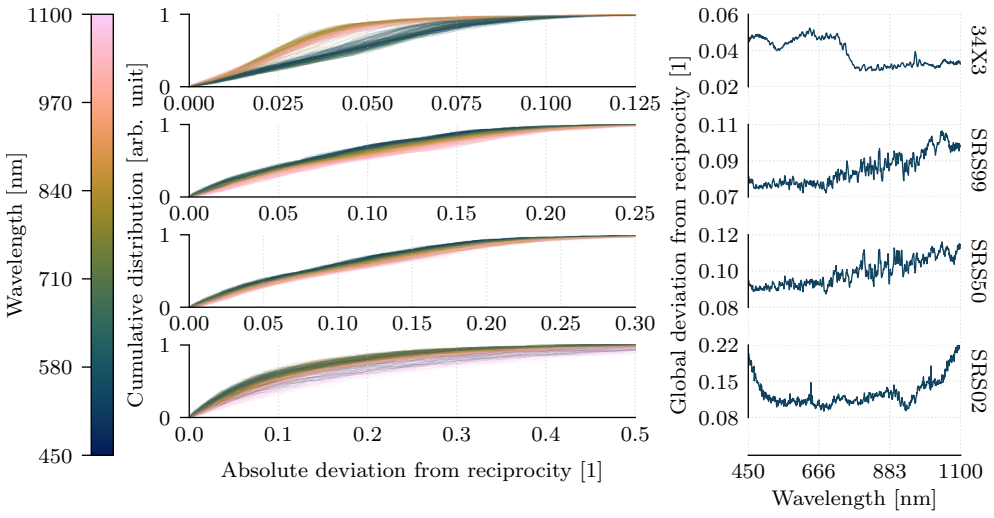

(a) (b)

Fig. 8. (a) CDFs computed for each wavelength for absolute deviation from reciprocity distributions for several samples. (b) Corresponding integrated CCDFs as functions of wavelength. The global deviation from reciprocity varies slightly as a function of wavelength, and is more correlated with the amplitude of the BRDF, decreasing with it as the measurement noise becomes more significant.

Optics EXPRESS

3.3. Conservation of energy

The computed DHR is presented for four samples (SRS99, SRS50, SRS02 in Fig. 9, 34X3 in Fig. 10) for which we have a reference DHR. The Spectralon reference values were supplied by the manufacturer LabSphere, while those for sample 34X3 were carried out by DGA Aeronautical Techniques [44,45] using a PerkinElmer Lambda 900 spectrophotometer with a 5 nm spectral step. All the results shown were measured, or computed from a BRDF measured at a 8-degree incidence.

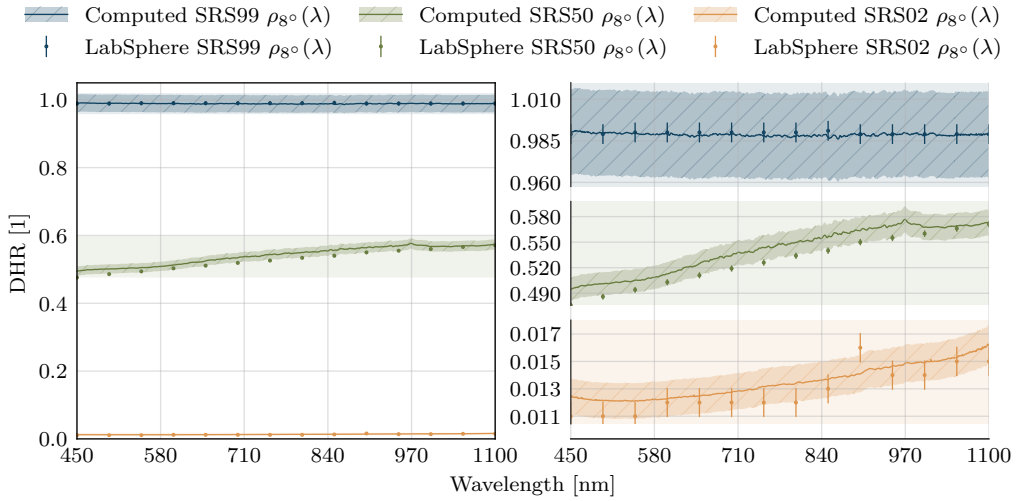

Fig. 9. Computed DHR and their uncertainties (lines and hatched areas) as a function of wavelength for three Spectralon compared with their DHR and uncertainties (dots with error bars) supplied by the manufacturer LabSphere. The graphs on the right are zoomed-in parts of the graph on the left. The correlation between the results obtained and the reference values enables the measurements on the bench to be validated.

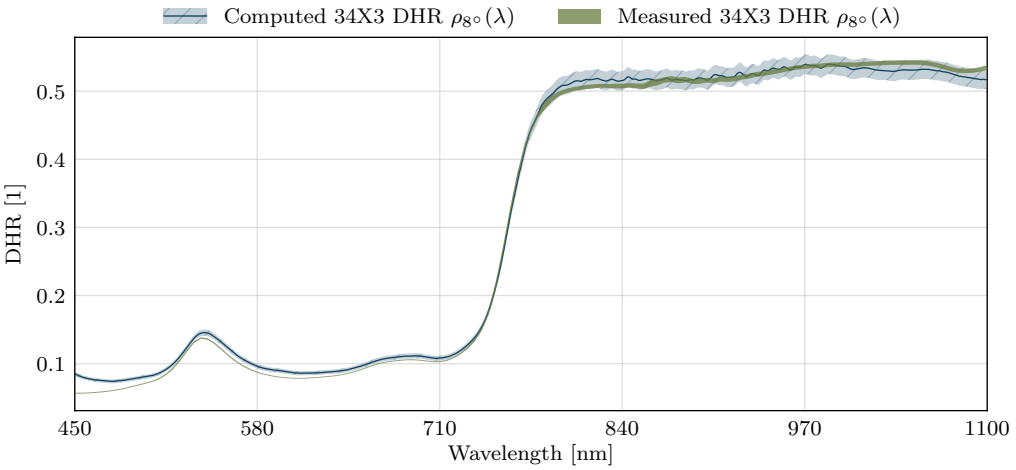

Fig. 10. Computed DHR and its uncertainty (lines and hatched areas) as a function of wavelength for the 34X3 sample with its measured DHR and its uncertainty (green area) supplied by DGA Aeronautical Techniques [44,45]. The correlation between the results and the reference values validates the approach for non-Lambertian samples.

Optics EXPRESS

3.4. Validity of the Lambertian hypothesis

The validity of the Lambertian hypothesis is calculated from Eq. (4). The calculated results are shown in Fig. 11. The graph on the left contains the four associated $\Lambda_{8^\circ}(\lambda)$ functions, all computed for a 8-degree incidence. Since the validity of the Lambertian hypothesis is much greater for Spectralon, the graph on the right gives a more accurate view of these three functions over a smaller codomain.

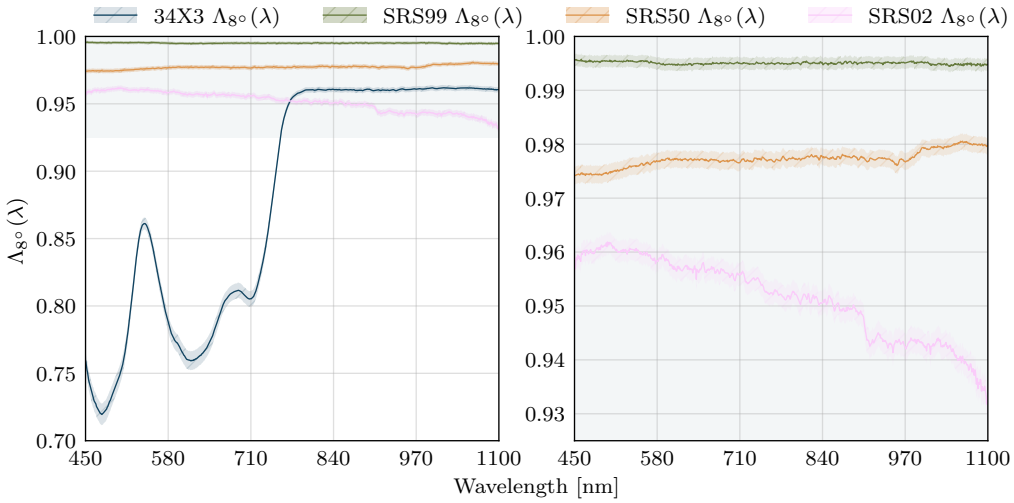

Fig. 11. Validity of the Lambertian hypothesis and its uncertainty (respectively lines and hatched areas) calculated for samples 34X3, SRS99, SRS50 and SRS02 from Eq. (4) at a 8-degree incidence. The graph on the right is a zoomed section of the graph on the left. A strong variation in the shape of the BRDF depending on wavelength can be seen for sample 34X3, rejecting the approximation $f(\omega_i, \omega_o, \lambda) = f_\omega(\omega_i, \omega_o) f_\lambda(\lambda)$. The hypothesis of Lambertian behaviour for Spectralon becomes less accurate for the darkest samples.

4. Discussion

4.1. Data analysis and interpretation

The processing chain shown in Fig. 3 produces a complete spectral isotropic BRDF dataset as shown in Fig. 5 for sample 34X3. Uncertainty calculations, both for the bench alignment and the BRDF value, have been controlled and are presented in Secs. 2.3.1 and 2.4 respectively. The former gave an alignment error of $\theta_n = (0.4\pm0.1)^\circ$, $\phi_n = (1.12\pm0.12)^\circ$, $\Delta z = (0.0\pm2.0)$ mm for this sample, with the vertical error Δz estimated at the time of measurement rather than using the method. As the method is based on the detection of the specular peak, it is not intended to be used for Lambertian samples. By observing the BRDFs of the Spectralons (Fig. 6), we can also see that there is sometimes significant variation at wide angles, particularly for the SRS50 sample (Fig. 6(e)). The most stable sample is logically SRS99 (Fig. 6(d)), our calibration sample.

The study of Helmholtz reciprocity on datasets measured in and out of the plane of incidence, as shown in Fig. 7, allows us to carry out an initial verification of the physical validity of our results. From a qualitative point of view, the histogram shows that the maxima of the distribution are not centred on a zero reciprocity error. This systematic error can be explained by a small misalignment of the bench, introducing a bias in the measurement of reciprocity. From a quantitative point of view, the CDFs and integrated CCDFs shown in Fig. 8 allow us to observe a weak dependence of reciprocity on wavelength. As can be seen from the curve for sample

Optics EXPRESS

34X3 Fig. 8(b), the overall deviation from reciprocity as a function of wavelength is related to the BRDF, with lower BRDF values introducing poorer reciprocity due to measurement noise. The shape of the BRDF, as characterised by the validity of the Lambertian hypothesis, is also correlated with reciprocity, with a Lambertian BRDF logically leading to a better measure of reciprocity.

A second check on the physical validity of our measurements can be made by observing the DHR calculated for each sample, as shown in Figs. 9 and 10. Figure 9, showing the DHRs obtained on every Spectralon, shows that our results are within the confidence interval of the reference values. Unsurprisingly, the values for the SRS99 sample match perfectly, this being used as the calibration sample. Figure 10, showing the results obtained for sample 34X3 compared with a reference measurement, enables us to judge the overall validity of our measurements. A deviation from the reference values can be seen at the limits of our spectral range, below 500 nm and above 1070 nm. While the two curves follow the same behaviour, there is probably a slight underestimation of our uncertainty for low DHR values.

Calculating the DHR also allows us to calculate the validity of the Lambertian hypothesis criterion Λ, as defined in Eq. (4) and shown in Fig. 11. For all the Spectralons, we can see that the Lambertian hypothesis is less valid for samples with a lower DHR. With the exception of sample SRS02, the value varies little as a function of wavelength. Looking at sample 34X3, although there is a relationship between the validity of the Lambertian hypothesis and the DHR, there is no correlation to be seen. This proves that this indicator is indeed an additional tool for characterizing BRDF, without being redundant with DHR.

As was pointed out when this criterion was introduced, however, it is not suitable for characterising the specular lobe itself of a material. Consequently, it will not be suitable for comparing the specular behaviour of two samples. The reader can be convinced of this by comparing the criterion for the validity of the Lambertian hypothesis for two simple theoretical BRDFs f_1 and f_2 such as $f_{1/2}(\omega_\mathrm{i}, \omega_\mathrm{o}) = k_\mathrm{s}\ \delta(\omega_\mathrm{o} - \omega_\mathrm{r})\ /\ \cos\theta_\mathrm{o} + k_{\mathrm{d},1/2}\ /\ \pi$. Although f_1 and f_2 have the same characteristic specular peak, calculating their criterion Λ will give a different result if $k_{\mathrm{d},1} \neq k_{\mathrm{d},2}$.

Since taking wavelength into account in BRDF measurement adds constraints to the device, and spectral BRDF models are rare [31], it is common practice to model materials using the approximation of a separable function $f(\omega_\mathrm{i}, \omega_\mathrm{o}, \lambda) = f_\omega(\omega_\mathrm{i}, \omega_\mathrm{o}) f_\lambda(\lambda)$ [46]. Observation of the results of spectral BRDF measurements as a function of both zenith angle and wavelength (Fig. 5(b)), as well as for the validity of the Lambertian hypothesis (Fig. 11), allows us to reject this approximation, and confirms the interest of a spectral BRDF measurement for this type of sample.

4.2. Directions for future work

Converting the measured spectral BRDF into RGB data could be useful for assessing the differences in rendering between a spectral rendering and an RGB rendering.

The current sampling of spectral BRDF observation directions could be enhanced to adapt more effectively to the BRDF measured. More advanced sampling is a serious area for improvement [47], that could allow both to improve the quality of output data and to reduce measurement time. In addition, if one wishes to use tabulated data to produce rendered images, the size of the files will be a significant problem (this point is discussed in more detail in the last paragraph of this section). A suitable sample would allow the file size to be optimised more effectively.

A post-process numerical realignment method for the setup is also an interesting area of improvement, as this bias is difficult to characterise and is a regular problem with this type of bench. The current method of calculating alignment error could be integrated into the processing chain for this purpose.

Optics EXPRESS

Future work on the measurement bench aims to extend the spectral observation range to 2500 nm. Polarization is also planned to be taken into account in the measurements, in order to trace the sample's Mueller matrix.

Integrating current measurements into a hyperspectral renderer while retaining the same spectral definition, or even extending it in the future, is likely to be a major implementation issue because of the size of the data: a tabulation of the spectral BRDF of a material with 90 points in incidence and zenith, with 180 points in azimuth without taking anisotropy into account and forcing bilateral symmetry, with a nanometric precision from 450 to 2500 nm in single precision would bring the dataset to 11.13 GByte. DGA Information Superiority has begun to explore this possibility in its work within the MSG-181 NATO group [48] and intends to continue based on the new method and results reported above. Using models instead of tabulated data is one possible approach, although it has been shown that a separable function model is unusable for certain materials. The criterion of validity of the Lambertian hypothesis is a potential tool that can be used as an effective property of material roughness obtained from BRDF measurements alone. It may subsequently be useful to propose a spectral BRDF model incorporating it in order to model the measured samples.

5. Conclusion

We have developed a gonio-scatterometer to characterize the spectral BRDF of materials from 450 to 1100 nm in and out of the plane of incidence with a spectral resolution of less than a nanometer. We have proposed a processing chain to study the physical validity of our measurements by studying non-negativity, Helmholtz reciprocity principle and the conservation of energy, having validated our setup by comparing our measurements with reference quantities. We have proposed and tested a method for calculating the alignment error for this type of bench, which can be easily improved to realign the data set numerically after measurement in the future. A new criterion for measuring validity of the Lambertian hypothesis has been introduced, allowing us to demonstrate that a separable function model can be inefficient for modelling certain materials. Future work could aim to use this observable as a parameter of an efficient model.

Funding. ONERA - The French Aerospace Lab; Région Sud Provence-Alps-French Riviera

Acknowledgments. The authors are grateful for the comments and guidance of the anonymous reviewers. The scientific colour maps used in this study prevent visual distortion of the data and exclusion of readers with colour-vision deficiencies [49]. The thumbnail image of this article is a computer-generated illustration.

Disclosures. The authors declare no conflicts of interest.

Data availability. Data underlying the results presented in this paper are not publicly available at this time but may be obtained from the authors upon reasonable request.

Supplemental document. See Supplement 1 for supporting content.

References

1. P. Ghamisi, N. Yokoya, J. Li, *et al.*, "Advances in hyperspectral image and signal processing: a comprehensive overview of the state of the art," IEEE Geosci. Remote Sens. Mag. **5**(4), 37–78 (2017).
2. E. Coiro, "Global illumination technique for aircraft infrared signature calculations," J. Aircr. **50**(1), 103–113 (2013).
3. H. Karimipour, J. K. O'Regan, and C. Witzel, "Sensory representation of surface reflectances: assessments with hyperspectral images," J. Opt. Soc. Am. A **40**(3), A183–A189 (2023).
4. C. D. Packard, T. S. Viola, and M. D. Klein, "Hyperspectral target detection analysis of a cluttered scene from a virtual airborne sensor platform using MuSES," in *Target and Background Signatures III*, (SPIE, 2017).
5. K. Krause, "Evaluation of Small-Footprint Full-Waveform Airborne Lidar Instrument Requirements Using DIRSIG Simulations of Forests," in *International Geoscience and Remote Sensing Symposium* (2020), pp. 6093–6096.
6. P. Boher, T. Leroux, L. Mignard-Debise, *et al.*, "Ray tracing simulation of one automotive display using spectroscopic polarized emissive and reflective measurements," SID Symp. Dig. Tech. Pap. **51**(1), 1445–1448 (2020).
7. M. Nimier-David, D. Vicini, T. Zeltner, *et al.*, "Mitsuba 2: A retargetable forward and inverse renderer," ACM Trans. on Graph. (TOG) **38**(6), 1–17 (2019).
8. D. Murray, A. Fichet, and R. Pacanowski, "Efficient Spectral Rendering on the GPU for Predictive Rendering," in *Ray Tracing Gems II*, (Apress, 2021), pp. 673–698.

Optics EXPRESS

9. M. Pharr, W. Jakob, and G. Humphreys, *Physically Based Rendering: From Theory to Implementation* (The MIT Press, 2023), 4th ed.
10. E. Coiro, C. Chatelard, G. Durand, *et al.*, "Experimental validation of an aircraft infrared signature code for commercial airliners," in *43rd AIAA Thermophysics Conference*, (New Orleans, Louisiana, 2012), p. 3190.
11. R. Hoarau, E. Coiro, S. Thon, *et al.*, "Interactive Hyper Spectral Image Rendering on GPU," in *VISIGRAPP*, (Funchal, Portugal, 2018), pp. 71–80.
12. Z. Mulhollan, A. Rangnekar, T. Bauch, *et al.*, "Calibrated vehicle paint signatures for simulating hyperspectral imagery," in *Proceedings of the IEEE/CVF Conference on Computer Vision and Pattern Recognition (CVPR) Workshops*, (2020), pp. 110–111.
13. M. D. Klein, M. T. Young, J. D. Taylor, *et al.*, "Sensitivity analysis of ResNet-based automatic target recognition performance using MuSES-generated EO/IR synthetic imagery," in *Synthetic Data for Artificial Intelligence and Machine Learning: Tools, Techniques, and Applications*, vol. 12529 (SPIE, 2023).
14. J. C. Perez, S. D. Vanstone, S. A. Acevedo, *et al.*, "Generating synthetic IR imagery to train modern deep learning detection and recognition algorithms to perform on similar real IR data," in *Synthetic Data for Artificial Intelligence and Machine Learning: Tools, Techniques, and Applications*, vol. 12529 (SPIE, 2023).
15. M. Bati, S. Blanco, C. Coustet, *et al.*, "Coupling conduction, convection and radiative transfer in a single path-space: Application to infrared rendering," ACM Trans. Graph. **42**(4), 1–20 (2023).
16. B. Duvenhage, K. Bouatouch, and D. G. Kourie, "Numerical verification of bidirectional reflectance distribution functions for physical plausibility," in *Proceedings of the South African Institute for Computer Scientists and Information Technologists Conference*, (2013), pp. 200–208.
17. M. da Silva Nunes, F. M. Nascimento, G. F. M. Jr., *et al.*, "Techniques for BRDF evaluation," Vis. Comput. **38**(2), 573–589 (2022).
18. S. R. Marschner, S. H. Westin, E. P. F. Lafortune, *et al.*, "Image-based bidirectional reflectance distribution function measurement," Appl. Opt. **39**(16), 2592–2600 (2000).
19. S.-H. Baek, T. Zeltner, H. J. Ku, *et al.*, "Image-based acquisition and modeling of polarimetric reflectance," ACM Trans. Graph. **39**(4), 1 (2020).
20. S. D. Butler, S. E. Nauyoks, and M. A. Marciniak, "Experimental measurement and analysis of wavelength-dependent properties of the BRDF," in *Imaging Spectrometry XX*, vol. 9611 (SPIE, 2015), pp. 78–92.
21. Z. Zhao, C. Qi, and J. Dai, "Design of multi-spectrum BRDF measurement system," Chin. Opt. Lett. **5**(3), 168–171 (2007).
22. L. C. Doan, J. R. Mahan, K. J. Priestley, *et al.*, "Measuring bidirectional reflectance distribution of low reflectivity surfaces in the near infrared," in *Optical Modeling and System Alignment*, vol. 11103 (SPIE, 2019), p. 111030I.
23. R. Baribeau, W. S. Neil, and E. Côté, "Development of a robot-based gonioreflectometer for spectral BRDF measurement," J. Mod. Opt. **56**(13), 1497–1503 (2009).
24. A. M. Rabal, A. Ferrero, J. Campos, *et al.*, "Automatic gonio-spectrophotometer for the absolute measurement of the spectral BRDF at in- and out-of-plane and retroreflection geometries," Metrologia **49**(3), 213–223 (2012).
25. S. Potin, O. Brissaud, P. Beck, *et al.*, "SHADOWS: a spectro-gonio radiometer for bidirectional reflectance studies of dark meteorites and terrestrial analogs: design, calibrations, and performances on challenging surfaces," Appl. Opt. **57**(28), 8279–8296 (2018).
26. W. Ma, Y. Liu, and Y. Liu, "The measurement and modeling investigation on the spectral polarized brdf of brass," Opt. Rev. **27**(4), 380–390 (2020).
27. M. Fouchier, M. Zerrad, M. Lequime, *et al.*, "Wide-range wavelength and angle resolved light scattering measurement setup," Opt. Lett. **45**(9), 2506–2509 (2020).
28. D. Lanevski, F. Manoocheri, and E. Ikonen, "Gonioreflectometer for measuring 3D spectral BRDF of horizontally aligned samples with traceability to SI," Metrologia **59**(2), 025006 (2022).
29. B. Raybaud, E. Vergnault, A. Disdier, *et al.*, "Identification of BRDF parameters with spectral measurements in the visible light spectrum towards solar irradiation evaluation in urban environment for photovoltaïc technologies," Energy and Buildings **263**, 112034 (2022).
30. S. Inoue, Y. Igarashi, T. Hoshi, *et al.*, "Measuring BRDF for curved surfaces based on parabolic reflection," Opt. Continuum **1**(8), 1637–1651 (2022).
31. D. Guarnera, G. C. Guarnera, A. Ghosh, *et al.*, "BRDF representation and acquisition," Computer Graphics Forum **35**(2), 625–650 (2016).
32. R. Ceolato, N. Riviere, and L. Hespel, "Reflectances from a supercontinuum laser-based instrument: hyperspectral, polarimetric and angular measurements," Opt. Express **20**(28), 29413–29425 (2012).
33. F. E. Nicodemus, "Directional reflectance and emissivity of an opaque surface," Appl. Opt. **4**(7), 767–775 (1965).
34. A. Broder and M. Henzinger, *Handbook of Massive Data Sets*, vol. 4 of *Massive Computing* (Springer, 2002).
35. F. Romeiro, Y. Vasilyev, and T. Zickler, "Passive Reflectometry," in *Computer Vision – ECCV 2008*, vol. 5305 of *Lecture Notes in Computer Science* (Springer, 2008), pp. 859–872.
36. T. V. Small, S. D. Butler, and M. A. Marciniak, "Augmenting CASI® BRDF measurement device to measure out-of-plane scatter with CCD pixel array," in *Reflection, Scattering, and Diffraction from Surfaces VII*, vol. 11485 (SPIE, 2020), p. 114850B.

Optics EXPRESS

37. J. F. Blinn, "Models of light reflection for computer synthesized pictures," in *Proceedings of the 4th Annual Conference on Computer Graphics and Interactive Techniques*, (Association for Computing Machinery, 1977), SIGGRAPH '77, pp. 192–198.
38. J. Filip, R. Vavra, M. Haindl, *et al.*, "BRDF Slices: Accurate Adaptive Anisotropic Appearance Acquisition," in *Proceedings of the IEEE Conference on Computer Vision and Pattern Recognition (CVPR)* (2013).
39. K. Omer and M. Kupinski, "Compression, interpolation, and importance sampling for polarized BRDF models," Opt. Express **30**(14), 25734–25752 (2022).
40. P. K. Mishra, S. K. Nath, M. K. Sen, *et al.*, "Hybrid Gaussian-cubic radial basis functions for scattered data interpolation," Comput. Geosci. **22**(5), 1203–1218 (2018).
41. H. H. Ku, "Notes on the use of propagation of error formulas," Journal of Research of the National Bureau of Standards **70**, 263–273 (1966).
42. N. Shklov, "Simpson's rule for unequally spaced ordinates," The Am. Math. Mon. **67**(10), 1022–1023 (1960).
43. K. E. Atkinson, *An Introduction to Numerical Analysis* (John Wiley & Sons, 1989), chap. 5.1, pp. 251–258, 2nd ed.
44. A. L. Goff, Y. Hurtaud, E. Floch, *et al.*, "First experiment with French CUBI object: analysis of measurements and initial simulation," in *International IR Target and Background Modeling & Simulation Works*, (2018), pp. 169–183.
45. A. L. Goff, Y. Hurtaud, E. Floch, *et al.*, "CUBI experiment & simulation for infrared scene modeling validation," in *International Symposium on Optronics in Defence and Security*, (2018), 37.
46. A. Ferrero, A. M. Rabal, J. Campos, *et al.*, "Variables separation of the spectral BRDF for better understanding color variation in special effect pigment coatings," J. Opt. Soc. Am. A **29**(6), 842–847 (2012).
47. T. Tongbuasirilai, J. Unger, and M. Kurt, "Efficient BRDF sampling using projected deviation vector parameterization," in *Proceedings of the IEEE International Conference on Computer Vision Workshops*, (2017), pp. 153–158.
48. A. Le Goff, "Advanced optical modelling of the 34X3 paint covering the DGA CUBI object," in *Simulation and Augmented Reality*, OPTRO (Association Aéronautique et Astronautique de France, 2024).
49. F. Crameri, G. E. Shephard, and P. J. Heron, "The misuse of colour in science communication," Nat. Commun. **11**(1), 5444 (2020).